Time domain room acoustic simulations using a spectral element method

Finnur Pind,[1, a)] Allan P. Engsig-Karup,[2] Cheol-Ho Jeong,[3] Jan S. Hesthaven,[4] Mikael S. Mejling,[2] and Jakob Strømann-Andersen[1]

[1] *Henning Larsen, Copenhagen, Denmark*

[2] *Scientific Computing Section, Department of Applied Mathematics and Computer Science, Technical University of Denmark, Kongens Lyngby, Denmark*

[3] *Acoustic Technology Group, Department of Electrical Engineering, Technical University of Denmark, Kongens Lyngby, Denmark*

[4] *Chair of Computational Mathematics and Simulation Science, Ecole polytechnique federale de Lausanne, Lausanne, Switzerland*

This paper presents a wave-based numerical scheme based on a spectral element method, coupled with an implicit-explicit Runge-Kutta time stepping method, for simulating room acoustics in the time domain. The scheme has certain features which make it highly attractive for room acoustic simulations, namely a) its low dispersion and dissipation properties due to a high-order spatio-temporal discretization, b) a high degree of geometric flexibility, where adaptive, unstructured meshes with curvilinear mesh elements are supported and c) its suitability for parallel implementation on modern many-core computer hardware. A method for modelling locally reacting, frequency dependent impedance boundary conditions within the scheme is developed, in which the boundary impedance is mapped to a multipole rational function and formulated in differential form. Various numerical experiments are presented, which reveal the accuracy and cost-efficiency of the proposed numerical scheme. [a]

 [http://dx.doi.org(DOI number)]

[XYZ] Pages: 1–14

Keywords: Room acoustic wave-based simulations, spectral element method, high-order numerical schemes, frequency dependent impedance boundary conditions

I. INTRODUCTION

Room acoustic simulations are used in many fields, for example in building design,[1] virtual reality,[2] entertainment,[3] automotive design,[4] music,[5] and hearing research.[6] Since their inception in the 1960's,[7,8] room acoustic simulations have primarily been carried out by means of *geometrical acoustics methods*,[9] such as the ray tracing method,[10] the image source method[11] or the beam tracing method.[12] In these methods, several simplifying approximations regarding sound propagation and reflection are made, which make the computational task more manageable. These approximations will, however, reduce the accuracy of the simulation because various important wave phenomena, such as diffraction, interference, phase and scattering are not accurately captured. Wave phenomena will be prominent in rooms where the room dimensions and sizes of obstacles are comparable to the wavelength of the acoustic wave. Small to medium sized rooms, and low to mid frequencies, are here of primary concern.[13] However, large rooms can also exhibit wave phenomena, the seat-dip effect is an example of this.[14] Another problem associated with geometrical acoustics methods is that they require simplified 3D models, made up of coarse planar polygons. Fine geometrical details are typically handled by assigning scattering coefficients to planar surfaces and these coefficients are often based on crude visual inspection.[15] Instead of using simplified 3D models, it would be more accurate to model directly the complex and detailed geometry typically found in architectural models.[16]

Thanks to the continuous advances in computation power and in scientific computing theory, the *wave-based methods* are becoming a viable alternative for room acoustic simulations. In these methods the governing physics equations are solved numerically, and they are therefore, from a physical point of view, more accurate than their geometrical counterparts, since all wave phenomena is inherently accounted for.[17] Wave-based methods that have been applied to room acoustic simulations include the finite-difference time-domain method (FDTD),[18] the boundary element method (BEM),[19] the linear finite element method (h-FEM),[20] the equivalent source method (ESM),[21] the finite volume method (FVM)[22] and the pseudospectral time-domain method (PSTD).[23] A major drawback of the wave-based meth-

a)fpin@henninglarsen.com

[a]A part of the results of this paper was previously presented at Euronoise 2018 in Creta.

ods is the large computational effort needed.[24] Various studies have been carried out to bring down computation times, e.g. parallel implementations of algorithms utilizing many-core hardware such as GPU's,[25] hybridization of different algorithm types,[4,26,27] and recently, the usage of high-order numerical methods, which have the potential of being cost-efficient,[28] has been investigated within the context of room acoustics.[29,30]

The primary purpose of this paper is to present a numerical scheme based on a spectral element method (SEM),[31–33] adapted for time domain room acoustic simulations, and to assess the suitability of using the SEM for this task. The SEM is known to be well-suited for cost-effective simulations of large scale problems over long simulation times due to a high-order polynomial basis discretization, which leads to small numerical dispersion and dissipation errors.[34] Furthermore, the SEM is capable of operating on unstructured, adaptive meshes with curvilinear mesh elements, making it highly suitable for simulating complex geometries. Finally, the SEM has also been shown to be well-suited for parallel computing.[35,36] In the scheme presented here, time stepping is done by means of an implicit-explicit high-order Runge-Kutta solver,[37] ensuring computational efficiency, robustness and the maintenance of global high-order accuracy. A method for incorporating locally reacting, frequency dependent impedance boundary conditions in the scheme is presented.

The SEM has several advantages compared to the other wave-based methods found in the literature. The FDTD method and the PSTD method are ill-suited for dealing with complex geometries.[38,39] The FVM overcomes this drawback of limited geometrical flexibility,[22] however, another challenge with the FVM is a flux reconstruction procedure that, despite recent progress, is not straightforward to extend to arbitrarily high-order accuracy in two and three spatial dimensions.[40,41] The BEM has the benefit of needing only to discretize the boundary surface instead of the domain volume, however, in the BEM operators are dense. Typically the FEM, which has sparse operators and where the domain volume is discretized, is considered faster than BEM unless the volume to surface area becomes very large.[24] In addition, there are other challenges relating to uniqueness of solutions in the BEM.[42] High-order FEM, typically referred to as the *hp*-FEM, is another option.[43] The *hp*-FEM and the SEM are based on the same underlying theoretical framework and possess similar properties, while differing in implementation. The key distinction between the *hp*-FEM and the SEM is whether the expansion is modal or nodal. In *hp*-FEM the expansion basis is normally modal, i.e. the basis functions are of increasing order (hierarchical). In a modal expansion the expansion coefficients do not have any particular physical meaning. In contrast, in SEM the expansion basis is a non-hierarchical Lagrange basis that consists of polynomials of order P. Importantly, the nodal expansion coefficients are associated with the solution values at the nodal points, hence these can be interpreted readily. The discontinuous Galerkin finite element method (DGFEM) is another method which stems from a similar theoretical framework as the SEM. Its main drawbacks relative to the SEM is that it requires more degrees of freedom, and a flux reconstruction between elements must be computed. However, it relies only on local weak formulations defined for elements rather than for the full domain as in the SEM, which makes it possible to exploit the resulting locality in parallelization. *hp*-FEM, SEM and DGFEM have similar geometric flexibility.[44]

II. GOVERNING EQUATIONS & BOUNDARY CONDITIONS

Acoustic wave propagation in a lossless medium in a d dimensional enclosure is governed by the following system of two coupled linear first-order partial differential equations,

$$\begin{aligned} \mathbf{v}_t &= -\frac{1}{\rho}\nabla p, \\ p_t &= -\rho c^2 \nabla \cdot \mathbf{v}, \end{aligned} \qquad \text{in } \Omega\times[0,t], \tag{1}$$

where $p(\mathbf{x},t)$ is the sound pressure, $\mathbf{v}(\mathbf{x},t)$ is the particle velocity, $\mathbf{x}$ is the position in space of the domain Ω, t is time, ρ is the density of the medium and c is the speed of sound in air ($\rho = 1.2\,\mathrm{kg/m^3}$ and $c = 343\,\mathrm{m/s}$ in this study). These equations correspond to the linearized Euler equations without flow. This system is exactly equivalent to the more commonly used second order wave equation.

Sufficient boundary conditions must be supplied with the system in Eq. (1), and in room acoustics it is natural to define the boundary conditions in terms of the complex, frequency dependent surface impedance $Z(\omega)$, which can be estimated from material models or from measurements.[45,46] The pressure and the particle velocity at the boundary are related through the surface impedance in the frequency domain via

$$\hat{v}_n(\omega) = \frac{\hat{p}(\omega)}{Z(\omega)} = \hat{p}(\omega)Y(\omega), \tag{2}$$

where ω is the angular frequency, $\hat{p}$ and $\hat{v}_n = \hat{\mathbf{v}}\cdot\mathbf{n}$ are the Fourier transforms of the pressure and particle velocity at the boundary, respectively, $\mathbf{n}$ is the surface normal unit vector and $Y(\omega)$ is the boundary admittance, which is convenient to use when implementing frequency dependent boundary conditions into the linearized Euler equations. The boundary admittance can be approximated as a rational function on the form

$$Y(\omega) = \frac{a_0 + \cdots + a_N(-j\omega)^N}{1 + \cdots + b_N(-j\omega)^N}, \tag{3}$$

which can be rewritten by using partial fraction decomposition as[47]

$$\begin{aligned} Y(\omega) =& Y_\infty + \sum_{k=1}^{Q} \frac{A_k}{\lambda_k - j\omega} \\ &+ \sum_{k=1}^{S} \left(\frac{B_k + jC_k}{\alpha_k + j\beta_k - j\omega} + \frac{B_k - jC_k}{\alpha_k - j\beta_k - j\omega} \right), \end{aligned} \tag{4}$$

where Q is the number of real poles λ_k and S is the number of complex conjugate pole pairs $\alpha_k \pm j\beta_k$, used in the rational function approximation. Y_∞, A_k, B_k, C_k are numerical coefficients. Any number of poles can be chosen, one strategy being to choose enough poles such that the error in the multipole approximation of the boundary admittance is below a predefined threshold.

Eq. (2) can be transformed to the time domain by means of an inverse Fourier transform,

$$v_n(t) = \int_{-\infty}^{t} p(t')y(t-t')\,dt'. \tag{5}$$

Then, by applying an inverse Fourier transform on Eq. (4) and inserting it into Eq. (5), the expression for the velocity at the boundary becomes

$$\begin{aligned} v_n(t) =& Y_\infty p(t) + \sum_{k=1}^{Q} A_k \phi_k(t) \\ &+ \sum_{k=1}^{S} 2\left[B_k \psi_k^{(1)}(t) + C_k \psi_k^{(2)}(t) \right], \end{aligned} \tag{6}$$

where ϕ_k, $\psi_k^{(1)}$ and $\psi_k^{(2)}$ are so-called accumulators. They are determined by the following set of ordinary differential equations

$$\begin{aligned} &\frac{d\phi_k}{dt} + \lambda_k \phi_k(t) = p(t), \\ &\frac{d\psi_k^{(1)}}{dt} + \alpha_k \psi_k^{(1)}(t) + \beta_k \psi_k^{(2)}(t) = p(t), \\ &\frac{d\psi_k^{(2)}}{dt} + \alpha_k \psi_k^{(2)}(t) - \beta_k \psi_k^{(1)}(t) = 0. \end{aligned} \tag{7}$$

This approach is often called the auxiliary differential equations (ADE) method in the literature,[47–49] and has the benefit of being computationally efficient, because solving a small set of linear ODE's requires only relatively minor computations. Furthermore, this approach has low memory requirements because no time history must be stored.

III. NUMERICAL DISCRETIZATION

In this section, a high-order numerical scheme for the solution of Eq. (1) in two and three spatial dimensions is derived. High-order methods are methods which have a global error convergence rate $\mathcal{O}(h^P)$ of at least third order ($P > 2$), where h is the mesh element side length. In this study, triangular mesh elements are used in 2D, and hexahedral elements are used in 3D, although elements of different shapes can be used.

A. Spatial discretization

The domain Ω is partitioned into a set of non-overlapping elements Ω_n, $n = 1, \ldots, N_{\text{el}}$. A set of nodes is chosen and mapped into each element, making up a total of K nodes across the mesh and having coordinates $\mathbf{x}_i$, $i = 1 \ldots K$. A finite element approximation space V of globally continuous, piece-wise polynomial functions of degree at most P is introduced, $V = \{\phi \in C^0(\Omega); \forall n \in \{1, \ldots, N_{\text{el}}\}, \phi^{(n)} \in \mathbb{P}^P\}$. As such, the global basis functions ϕ are defined by patching together local polynomial nodal basis functions $\phi^{(n)}$, which are defined locally on each element and in this study taken to be Lagrange polynomials of order P. To support order P basis functions, each element must contain $K_P = (P+1)(P+2)/2$ nodes in 2D for the triangular elements and $K_P = (P+1)^3$ nodes in 3D for the hexahedral elements.[44] Fig. 1 shows an example of a 2D mesh of a rectangular domain, supporting $P = 4$ order basis functions.

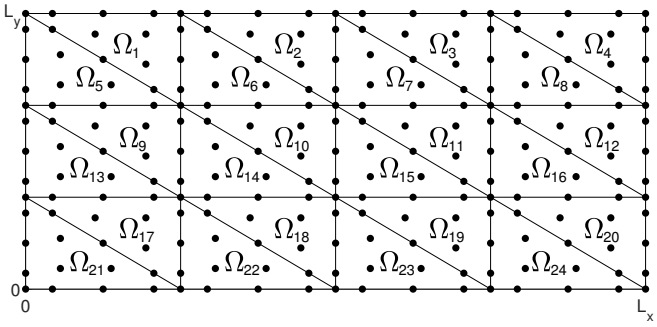

FIG. 1. An example of a mesh of a 2D rectangular domain, using triangular elements and having nodes for supporting $P = 4$ basis functions. The mesh is made up of $N_{\text{el}} = 24$ elements and contains 221 DOF's (nodes).

The weak formulation of the governing equations, through the use of the Divergence theorem on the pressure equation in Eq. (1), takes the following form

$$\begin{aligned} &\int_\Omega \mathbf{v}_t \phi \, \mathrm{d}\Omega = -\frac{1}{\rho} \int_\Omega \nabla p \; \phi \, \mathrm{d}\Omega, \\ &\int_\Omega p_t \phi \, \mathrm{d}\Omega = -\rho c^2 \left[\int_\Gamma \phi \hat{\mathbf{n}} \cdot \mathbf{v} \, \mathrm{d}\Gamma - \int_\Omega \mathbf{v} \cdot \nabla \phi \, \mathrm{d}\Omega \right], \end{aligned} \tag{8}$$

where Γ denotes the boundary of Ω. Now, introduce a truncated series expansion for the unknown variables $\mathbf{v}$ and p in Eq. (8)

$$\begin{aligned} \mathbf{v}(\mathbf{x}, t) &\approx \sum_{i=1}^{K} \hat{\mathbf{v}}_i(t) N_i(\mathbf{x}), \\ p(\mathbf{x}, t) &\approx \sum_{i=1}^{K} \hat{p}_i(t) N_i(\mathbf{x}), \end{aligned} \tag{9}$$

where $N_i(\mathbf{x}) \in V$ is the set of global finite element basis functions, possessing the cardinal property $N_i(\mathbf{x}_j) = \delta_{ij}$.

Substituting the approximations in Eq. (9) for $\mathbf{v}$ and p into Eq. (8) and choosing $\phi \in \{N_i(\mathbf{x})\}_{i=1}^{K}$ to define a nodal Galerkin scheme results in the following semi-discrete system

$$\begin{aligned} Mv_x' &= -\frac{1}{\rho} S_x p, \quad Mv_y' = -\frac{1}{\rho} S_y p, \quad Mv_z' = -\frac{1}{\rho} S_z p, \\ Mp' &= \rho c^2 \left(S_x^T v_x + S_y^T v_y + S_z^T v_z - v_n B \right), \end{aligned} \tag{10}$$

where v_x, v_y, v_z represent the x, y, z components of the particle velocity, v_n is computed using Eq. (6) and where the following global matrices have been introduced

$$\begin{aligned} M_{ij} &= \int_\Omega N_j \; N_i \;\; \mathrm{d}\Omega, \quad S_{x,(ij)} = \int_\Omega (N_j)_x \; N_i \;\; \mathrm{d}\Omega, \\ S_{y,(ij)} &= \int_\Omega (N_j)_y \; N_i \;\; \mathrm{d}\Omega, \quad S_{z,(ij)} = \int_\Omega (N_j)_z \; N_i \;\; \mathrm{d}\Omega, \\ B_{ij} &= \int_\Gamma N_j \; N_i \;\; \mathrm{d}\Gamma \end{aligned} \tag{11}$$

where the x, y, z subscripts in the integrals denote differentiation. In Eq. (10) M is typically called the mass matrix and S is called the stiffness matrix. To determine these matrices, it is convenient to introduce the concept of a local *element matrix*.

Due to the nature of the global piece-wise basis functions, the integrals in Eq. (11) are only non-zero when the nodes i, j belong to the same element.[32] This means that two basis functions N_i and N_j only contribute towards entries M_{ij} when $x_i, x_j \in \Omega_n$, due to the local support of the basis functions. This leads to the definition of the local element matrices as

$$\begin{aligned} \mathcal{M}_{ij}^{(n)} &= \int_{\Omega_n} N_i^{(n)} \; N_j^{(n)} \, \mathrm{d}\Omega_n, \\ \mathcal{S}_{x,(ij)}^{(n)} &= \int_{\Omega_n} N_i^{(n)} \; (N_j^{(n)})_x \, \mathrm{d}\Omega_n, \\ \mathcal{S}_{y,(ij)}^{(n)} &= \int_{\Omega_n} N_i^{(n)} \; (N_j^{(n)})_y \, \mathrm{d}\Omega_n, \\ \mathcal{S}_{z,(ij)}^{(n)} &= \int_{\Omega_n} N_i^{(n)} \; (N_j^{(n)})_z \, \mathrm{d}\Omega_n, \\ & i, j = 1 \dots K_P. \end{aligned} \tag{12}$$

From the local element matrices, it is possible to assemble the global matrices in Eq. (11) by iterating over the elements and summing the element contributions relying on the property of domain decomposition, e.g.

$$M_{ij} = \int_\Omega N_i N_j \, d\Omega = \sum_{n=1}^{N_{el}} \int_{\Omega_n} N_i^{(n)} N_j^{(n)} \, d\Omega_n, \tag{13}$$

where the integrals may be zero, cf. discussion above. The element matrices are therefore dense, whereas the global matrices are sparse.

B. Spatial integration and nodal/modal duality

To compute the element matrices in Eq. (12), it is convenient to introduce a special element called the reference element Ω_r. In 2D it is a triangle, given by

$$\mathcal{I}^2 = \left\{ \mathbf{r} = (r, s) | (r, s) \geq -1; r + s \leq 0 \right\}, \tag{14}$$

and in 3D it is a hexahedron, given by

$$\mathcal{I}^3 = \left\{ \mathbf{r} = (r, s, t) | -1 \leq (r, s, t) \leq 1 \right\}. \tag{15}$$

On these elements one can define a hierarchical modal basis, as opposed to the nodal basis discussed above. This implies a possible modal/nodal duality in the representation of the local solutions that can be exploited for exact integration, relying on the orthogonal properties of the local modal basis functions without resorting to numerical quadrature rules. When using a modal basis, an unknown function is represented as

$$u(\mathbf{r}) = \sum_{j=0}^{P} \tilde{u}_j \psi_j(\mathbf{r}), \quad \mathbf{r} \in \mathcal{I}^d, \tag{16}$$

where ψ_j are the modal basis functions and the coefficients $\tilde{u}_j$ are weights. On $\mathcal{I}^2$ a basis proposed by Dubiner[50] is chosen, where the reference triangle element is first mapped to a unit square quadrilateral element by the mapping

$$T : (r, s) \to (a, b), \; T(r, s) = \left(2 \frac{1 + r}{1 - s} - 1 \; , \; s \right), \tag{17}$$

where (a, b) are the coordinates in the quadrilateral element. This allows for defining a modal basis in terms of tensor products from the 1D reference element $\mathcal{I}^1 = [-1, 1]$. The intra-element nodal distribution of the collocation points $\mathbf{r}$ of the 1D reference element used in this study is of the Legrende-Gauss-Lobatto (LGL) kind. Using this nodal distribution avoids Runge's phenomenon.[44] Now, the 2D modal basis is defined as

$$\psi_{pq}(r, s) = \phi_p^a(r) \; \phi_q^b(s), \tag{18}$$

where

$$\phi_p^a(r) = \mathcal{P}_p^{0,0}(r), \quad \phi_q^b(s) = \left(\frac{1 - s}{2} \right)^2 \mathcal{P}_q^{2p+1,0}(s), \tag{19}$$

and where $\mathcal{P}_p^{\alpha,\beta}(z)$ is the p'th order Jacobi polynomial with parameters α, β. By constructing the basis functions ψ_{pq} in this manner they become orthonormal on $\mathcal{I}^2$.

On $\mathcal{I}^3$, a similar orthonormal modal basis is constructed using a tensor product of Jacobi polynomials

$$\begin{aligned} \psi(r, s, t) &= \mathcal{P}_i^{0,0}(r) \; \mathcal{P}_j^{0,0}(s) \; \mathcal{P}_k^{0,0}(t), \\ & i, j, k = 0 \dots P. \end{aligned} \tag{20}$$

The function values of the nodes $\hat{\mathbf{u}}$ used in the nodal representation and the weights $\tilde{\mathbf{u}}$ used in the modal representation of u relate to each other through

$$\mathcal{V} \hat{\mathbf{u}} = \tilde{\mathbf{u}}, \tag{21}$$

where $\mathcal{V}$ is the generalized Vandermonde matrix with

$$\mathcal{V}_{ij} = \psi_j(\mathbf{r}_i), \quad i,j = 1 \dots P+1. \tag{22}$$

Utilizing this, the i'th local nodal basis function on the reference element can be expressed as[44]

$$N_i(\mathbf{r}) = \sum_{n=1}^{P+1} \left(\mathcal{V}^T\right)^{-1}_{i,n} \psi_n(\mathbf{r}). \tag{23}$$

Inserting Eq. (23) into the expression defining the element mass matrix $\mathcal{M}$ on the reference element yields

$$\mathcal{M}_{ij} = \sum_{n=1}^{P+1} \left(\mathcal{V}^T\right)^{-1}_{i,n} \left(\mathcal{V}^T\right)^{-1}_{j,n} = \left(\mathcal{V}\mathcal{V}^T\right)^{-1}, \tag{24}$$

using the orthonormality of the chosen modal basis and thus avoiding the use of numerical quadrature rules. The connection to the mass matrix in Eq. (12) is defined by the coordinate mapping between reference element and any element in the physical space

$$\mathcal{M}^{(n)}_{ij} = \int_{\Omega_n} \psi_i(\mathbf{x})\psi_j(\mathbf{x}) d\Omega_n = \int_{\Omega_r} J^{(n)} \psi_i(\mathbf{r})\psi_j(\mathbf{r}) d\Omega_r. \tag{25}$$

where $\mathcal{J}^{(n)}$ is the Jacobian of the coordinate mapping $\xi : \mathbf{x}^{(n)} \rightarrow \mathbf{r}$.

Next, write the derivative of the i'th local basis function as

$$\frac{\partial}{\partial r} N_i(r,s,t) = \sum_{n=1}^{P+1} \frac{\partial}{\partial r} N_i(r_n, s_n, t_n)\ N_n(r,s,t). \tag{26}$$

Inserting the above into the expression defining the element stiffness matrix in Eq. (12) one finds that[44]

$$\mathcal{S}_r = \mathcal{M}\mathcal{D}_r, \tag{27}$$

where

$$\mathcal{D}_r = \mathcal{V}_r \mathcal{V}^{-1}, \tag{28}$$

is a differentiation matrix and

$$\mathcal{V}_{r,(ij)} = \frac{\partial}{\partial r} \psi_j(r_i, s_i). \tag{29}$$

The remaining element matrices $\mathcal{S}_s$ and $\mathcal{S}_t$ are defined similarly, and again the Jacobian coordinate mapping is used to map between the reference element and an arbitrary element in the mesh.

C. Time stepping and stability

In order to solve the ODE system in Eq. (10) efficiently, an explicit time stepping method is preferred.[51] Explicit time stepping comes with conditional stability, which sets an upper bound on the time step size Δt. In the proposed numerical scheme there are two mechanisms at play which influence the maximum allowable time step. Firstly, the usual global Courant-Friedrichs-Lewy (CFL) condition, where $\Delta t \leq C_1 / \max|\lambda_i|$, where λ_i represents the eigenvalues of the spatial discretization,[34] and C_1 is a constant depending on the size of the stability region of the time stepping method. Secondly, the stiffness of the ADE equations (Eq. (7)). For certain boundary conditions, the ADE equations can become stiff, which puts an excessively strict restriction on the time step. This motivates the usage of an implicit-explicit time stepping method, where the main SEM semi-discrete system (Eq. (10)) is integrated explicitly in time, whereas the ADE's, which are trivial to solve, are integrated implicitly in time. This way, the time step size is dictated solely by the global CFL condition, not by the boundary ADE's.

A six stage, fourth order implicit-explicit Runge-Kutta time stepping method is used. Let $F^{\text{ex}}(u,t)$ be a spatial discretization operator representing the right hand side of the main semi-discrete system, i.e. $u_t = F^{\text{ex}}(u,t)$, which is to be solved explicitly. Similarly, let $F^{\text{im}}(w,t)$ represent the right hand side of the ADE equations, i.e. $w_t = F^{\text{im}}(w,t)$, which are to be solved implicitly. Intermediate stages are calculated with

$$\begin{aligned} T_i &= t^n + c_i \Delta t \\ U_i &= u^n + \Delta t \sum_{j=1}^{6} a^{\text{ex}}_{ij} F^{\text{ex}}(U_j, T_j) \\ W_i &= w^n + \Delta t \sum_{j=1}^{6} a^{\text{im}}_{ij} F^{\text{im}}(W_j, T_j) \end{aligned} \tag{30}$$

and the next iterative step of the solution is given by

$$\begin{aligned} t^{n+1} &= t^n + \Delta t \\ u^{n+1} &= u^n + \Delta t \sum_{j=1}^{6} b^{\text{ex}}_{ij} F^{\text{ex}}(U_j, T_j) \\ w^{n+1} &= w^n + \Delta t \sum_{j=1}^{6} b^{\text{im}}_{ij} F^{\text{im}}(W_j, T_j) \end{aligned} \tag{31}$$

The coefficients $a^{\text{ex}}, a^{\text{im}}, b^{\text{ex}}, b^{\text{im}}, c$ can be found in[37].

For the SEM, the eigenvalues λ_i scale with polynomial order P in the following way[34]

$$\max|\lambda_i| \sim C_2 P^{2\gamma}, \tag{32}$$

where γ is the highest order of differentiation in the governing equations ($\gamma = 1$ here) and the constant C_2 is dependent on the minimum element size in the mesh. This means that using a very high polynomial order P, results only in marginal benefits in cost-efficiency due to a severe restriction on the time step size.

The temporal step size in 2D used in this work is given by[44]

$$\Delta t = C_{\text{CFL}} \min(\Delta r_i) \min \frac{r_D}{c}, \tag{33}$$

where Δr_i is the grid spacing between the LGL nodes in the reference 1D element $\mathcal{I}^1 = [-1, 1]$ and $r_D = \frac{A}{s}$ is the

radius of the triangular elements' inscribed circle, where s is half the triangle perimeter and A is the area of the triangle. Here $\min(\Delta r_i) \propto 1/P^2$ and $\min \frac{r_D}{c}$ corresponds the smallest element on the mesh, thus the expression scales in accordance with the conditional stability criterion described above. The constant C_{CFL} is on the order of $\mathcal{O}(1)$.

In the 3D case, the temporal step size is given by

$$\Delta t = C_{\mathrm{CFL}} \frac{\min\left(\Delta x,\, \Delta y,\, \Delta z\right)}{c}, \tag{34}$$

where $\Delta x, \Delta y$ and Δz are the grid spacings between nodes on the mesh in each dimension. Because the intra-element nodal distribution within each hexahedral element is based on LGL nodes, this expression also scales inversely with basis order P^2 and with element size, thus scaling proportionally to the stability criterion. Again the constant C_{CFL} is on the order of $\mathcal{O}(1)$.

IV. NUMERICAL PROPERTIES OF THE SCHEME

A. Numerical errors

Numerical errors will arise both due to the spatial discretization and the temporal discretization. These errors will be a mixture of dispersion errors and dissipation errors. An error convergence test is presented using a 3D cube domain of size $(1 \times 1 \times 1)\lambda$, where λ represents wavelength. The domain has periodic boundaries and is meshed uniformly with hexahedral elements. The error is defined as $\epsilon = \langle ||p_{\mathrm{a}} - p_{\mathrm{SEM}}||_{L_2} \rangle$. The L_2 integration is carried out numerically, by using the global mass matrix M as an integrator and $\langle\rangle$ indicates time averaging, such that the mean of the L_2 error across all time steps is taken. The analytic solution is given by

$$\begin{aligned} p_{\mathrm{a}}(x,y,z,t) = &\sin(2\pi(x-ct)) + \sin(2\pi(x+ct)) \\ &+ \sin(2\pi(y-ct)) + \sin(2\pi(y+ct)) \\ &+ \sin(2\pi(z-ct)) + \sin(2\pi(z+ct)). \end{aligned} \tag{35}$$

The domain is excited by an initial pressure condition, by setting $t = 0$ in the equation above. Mass lumping is used in the simulation to improve computational efficiency, see discussion on mass lumping in Sec. IV B. Fig. 2a shows the results of the convergence test for various polynomial orders P. Here the time step is set to be small enough ($C_{\mathrm{CFL}} = 0.01$ in Eq. (34)) such that spatial truncation errors dominate. The results show how fast the numerical errors decrease for different orders P, as the mesh element side length h is refined. For a given mesh element size, it is evident how the high-order basis functions result in significantly lower numerical errors.

In order to give insights into the effects of the temporal errors, another convergence test is carried out using a larger time step, having $C_{\mathrm{CFL}} = 0.75$ in Eq. (34). The results are shown in Fig. 2b. The global error convergence is unaffected for basis functions orders up to $P = 4$, but for $P > 4$ a loss of convergence rates is seen, as expected, since the time stepping method is only fourth-order accurate.

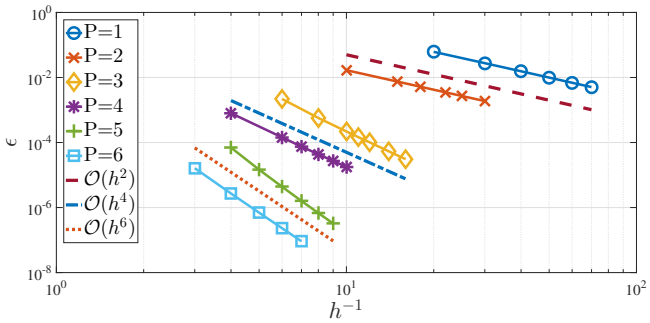

a) $C_{\mathrm{CFL}} = 0.01$.

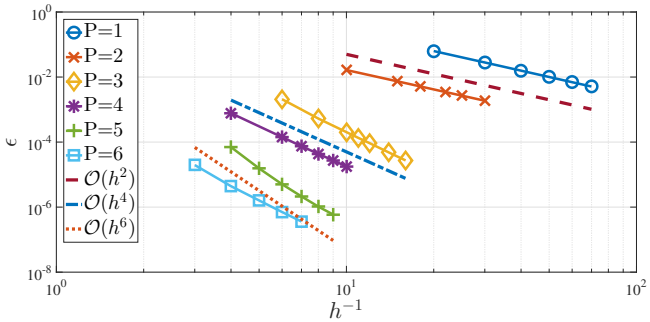

b) $C_{\mathrm{CFL}} = 0.75$.

FIG. 2. (Color online) Convergence test for the 3D periodic domain problem.

The dispersive and dissipative properties of the SEM for wave problems have been widely studied.[52–59] A commonly used approach for analyzing these properties in finite element methods for wave problems uses eigenvalue analysis. The eigenvalue analysis has been used to prove that the SEM is non-dissipative for wave problems.[53] However, numerical dissipation can be introduced via the time stepping method which is coupled with the SEM. The numerical dissipation of the complete scheme can be quantified by measuring the energy in the system under rigid boundary conditions, given by

$$E(t) = \int_{\Omega} \frac{1}{2\rho c^2} p(t,\mathbf{x})^2 + \frac{\rho}{2} |\mathbf{v}(t,\mathbf{x})|^2 \; d\mathbf{x}, \tag{36}$$

and a discrete measure of the energy can be computed in 3D by

$$\begin{aligned} E(t_n) = &\frac{1}{2\rho c^2} p^T M p \\ &+ \frac{\rho}{2} \left(v_x^T M v_x + v_y^T M v_y + v_z^T M v_z \right), \end{aligned} \tag{37}$$

where the global mass matrix M is employed as a quadrature free integrator. The dissipative properties of the proposed scheme are tested numerically in Sec. V B.

Using the eigenvalue analysis to analyze the dispersive properties of the SEM results in some ambiguity due to multiple solutions of the eigenvalue problem. A more

complete approach is a so-called a *multi-modal analysis*, where all of the numerical modes are regarded as relevant modes of wave propagation, relying on the representation of the numerical solutions in terms of a weighted combination of all the various numerical modes.[57,60] In this study, a multi-modal analysis method is devised, based on the 1D advection equation, which is representative of the single modes in the Euler equations,

$$u_t + cu_x = 0. \tag{38}$$

Exact solutions of the 1D advection equation can be stated on the general form

$$u(x,t) = f(kx - \omega t) = f((\omega/c)x - \omega t), \tag{39}$$

where $f(s)$ is any smooth function describing the initial condition waveform. Thus the initial condition takes the form

$$u^0 = u(x,0) = f((\omega/c)x). \tag{40}$$

By assuming a solution ansatz $f(s) = e^{js}$ for a single wave, the exact solution after N time steps will have a phase shift corresponding to $e^{-\omega N \Delta t}$. Knowing this, a relation between the numerical solution at time step N, u^N, and the initial condition u^0 can be established through

$$u^0 = u^N e^{-\hat{\omega} N \Delta t}, \tag{41}$$

where $\hat{\omega}$ is the numerical frequency, which will differ from the exact frequency ω due to the dispersion of the numerical scheme. This non-linear equation can be solved numerically for $\hat{\omega}$, in this study a Levenberg-Marquardt algorithm is used for this task, and by comparing the numerical frequency against the exact one, the dispersion relationship can be established since $c_d/c = \hat{w}/w$, where c_d is the numerical wave speed. This analysis comes with the advantage that any numerical simulator that solves the problem to evaluate u^N can be used and in this way all dispersive properties, spatial and temporal, of the given numerical scheme are taken into account. Fig. 3 shows a resulting dispersion relation, for a given spatio-temporal resolution. Clearly, the high-order discretization results in reduced dispersion errors. In 3D, fundamentally the same dispersion behavior will occur as in 1D, although here the dispersion relations will be dependent on the wave propagation direction.[59]

B. Computational work effort & mass lumping

As has been shown above, the usage of high-order basis functions results in lower numerical errors for a given mesh resolution, meaning that coarser spatial resolutions can be employed in simulations, thereby reducing computational cost significantly. However, when using explicit time stepping, the temporal step size must be made smaller when using high-order basis functions, as described in Sec. III C. This counterbalances the benefits of the coarser spatial mesh to a degree. The relevant question then becomes: for a given problem, which order of basis functions results in the most cost-effective simulation? The optimal order will primarily depend on the

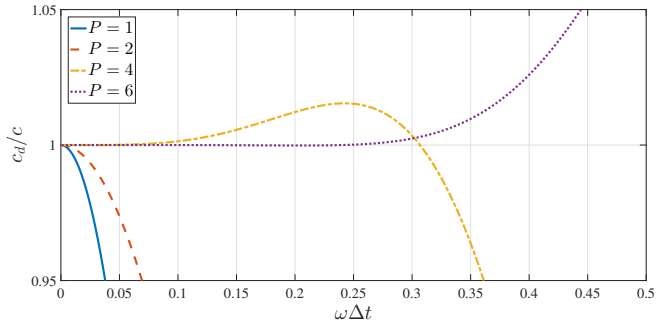

FIG. 3. (Color online) Numerical dispersion relations in 1D by means of a multi-modal analysis. $h = 0.1$, $\Delta t = 0.05$ and $c = 1$.

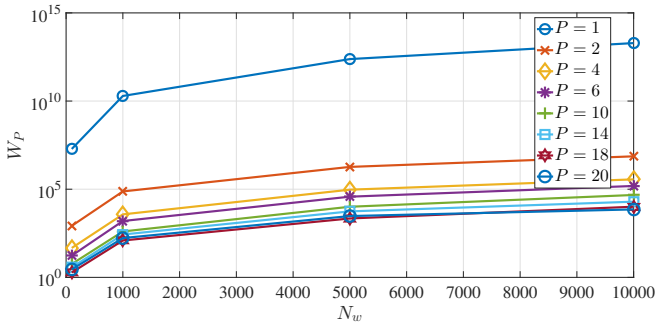

FIG. 4. (Color online) Predicted relative computational cost required to propagate a 3D wave on a periodic cube domain while maintaining an error tolerance $\epsilon = 0.02$.

desired numerical accuracy, the simulation time (room impulse response length) and the highest frequency of interest.[28]

A simple measure which can give an indication of the computational cost is applied in this study. The cost is defined as

$$W_P = N_{\text{timestep}} \cdot N_{\text{DOF,3D}}. \tag{42}$$

This model assumes serial computations and does not consider details such as matrix operator densities, computer architecture and implementation details. The $N_{\text{DOF,3D}}$ is evaluated from 1D numerical experiments, in which a 1D periodic domain of length 8λ, a lumped mass matrix and a time step size $\Delta t = \frac{3}{4}\frac{\min \Delta x}{c}$ is employed, under the assumption that the same spatial resolution is needed in 1D as in the axial directions in 3D. This way, $N_{\text{DOF,3D}} = N^3_{\text{DOF,1D}}$.

Fig. 4 shows the estimated relative computational cost required by the different orders to propagate a wave in a 3D periodic domain with $\epsilon = 2\%$ numerical accuracy, as a function of the simulation time, measured in wave periods N_w. The choice of $\epsilon = 2\%$ is ascribed to the audibility threshold for dispersion error.[61] The number of wave periods N_w in a periodic domain can be related to the impulse response length t_{IR} and the highest

frequency of interest f_h through $N_w = f_h t_{IR}$. The figure highlights a number of important properties of the scheme. For $P = 1$, which corresponds to the classic linear h-FEM, the computational cost is vastly larger compared to the other basis function orders. As the basis order P is increased, the efficiency improvement follows a trend of diminishing returns. Furthermore, the benefits of using high-order basis functions increases with simulation time. Comparing the computational cost for this particular test case for the $P > 1$ cases against the $P = 1$ case, shows that speed-up factors in the range of 10^4 to 10^9 can be expected, depending on which value of P is used and what simulation time is used. Comparing $P > 2$ against $P = 2$ shows speed-up factors in the range of 20 to 1000. However, it should be emphasised that this is based on a simplified measure of the computational cost and in reality other factors besides the spatial resolution and the number of time steps taken, e.g. those mentioned above, will influence the cost as well.

Mass lumping can be used to improve the efficiency of the scheme.[62] The global mass matrix M is made diagonal, rendering matrix multiplication trivial. Mass lumping will reduce accuracy slightly, but global convergence rates are maintained.[63] The SEM, when used in conjunction with quadrilateral elements in 2D and hexahedral elements in 3D, allows for the usage of mass lumping techniques in a straightforward way, namely

$$M_{ii} = \text{diag} \sum_j M_{ij}. \tag{43}$$

Applying mass lumping for meshes based on triangular elements in 2D and on tetrahedrons in 3D is more challenging, although one can take inspiration from previous studies.[64] In this study mass lumping is employed for all 3D simulations, whereas all 2D simulations are done without the use of mass lumping.

A simple test case is presented to demonstrate the trade-offs in accuracy and efficiency when using mass lumping. In this test case, $P = 4$. Table I shows a comparison of numerical errors ϵ and measured CPU times when simulating 100 wave periods on the 3D periodic domain. The CPU times are measured using a sequential, non-optimized, proof-of-concept implementation of the numerical scheme on an Intel Xeon E5-2650v4 CPU.

N_{el} per dim. / DOF	$\epsilon_{\text{Non-ML}}$	$t_{\text{Non-ML}}$	ϵ_{ML}	t_{ML}
2 / 512	0.1065	17 s	0.2815	9 s
3 / 1728	0.0217	269 s	0.0283	56 s
4 / 4096	0.0070	1617 s	0.0077	192 s
5 / 8000	0.0029	7314 s	0.0030	579 s

TABLE I. Numerical error ϵ and CPU times t with and without mass lumping, for $P = 4$ while simulating 100 wave periods on a periodic 3D cube domain.

The results show that the numerical error is slightly increased when mass lumping is used. The computation time, however, is significantly shorter when using mass lumping. It becomes more beneficial to use mass lumping on larger problems. In another test case where an error bound of $\epsilon = 1\%$ is used, simulating 100 wave periods with four mesh elements in each spatial dimension, the ML version is about 8 times faster than the non-ML version.

V. SIMULATION RESULTS

A. 2D circular domain

Consider a 2D circular domain with radius $a = 0.5$ m, centered at $(0, 0)$ m and having perfectly rigid boundaries. This test case is chosen to illustrate the geometric flexibility of the SEM. The impulse response of a given source-receiver pair is simulated for two cases, one using typical straight-sided triangular mesh elements, and another where the boundary elements have been transformed to be curvilinear. Fig. 5 shows the straight-sided mesh. When using straight-sided mesh elements, as is typically done in FEM simulations, a curved domain boundary will be poorly represented unless an extremely fine mesh is used, which leads to an undesirably high computational cost. The main benefit of using high-order numerical schemes is the ability to use a coarser mesh with large mesh elements, without a reduction in accuracy. By utilizing curvilinear mesh elements, it becomes possible to use large mesh elements with high basis orders, while at the same time capturing important geometrical details.

In both cases $P = 4$ basis functions are used and a relatively fine spatial resolution is employed, roughly 9 points per wavelength (PPW) for the highest frequency of interest (1 kHz). This means that only minimal dispersion should occur. The initial condition is a Gaussian pulse with spatial variance $\sigma = 0.05$ m^2, the simulation time is 3 s and the time step size is computed using Eq. (33) with $C_{\text{CFL}} = 0.75$.

Fig. 6 shows the simulated frequency responses, obtained via Fourier transforms of the simulated impulse responses. The curvilinear approach results in a better prediction of the analytic modes. For the straight-sided elements case, there is an apparent mistuning of the simulated modal frequencies, and this mistuning increases with frequency. Fig. 7 shows the difference in modal frequencies when comparing simulated versus analytic modal frequencies.

B. 3D cube room with rigid boundaries

Consider now a 3D $1 \times 1 \times 1$ m cube shaped room with perfectly rigid boundaries. The rigid cube is a test case of interest because an analytic solution exists, which simulations can be compared against.[67] The room impulse response is simulated for a given source-receiver pair using basis orders $P = 1, 2, 4, 6$. In all cases the spatial resolution is made to be the same, i.e. the number of DOF's on the mesh are fixed at 15,625, such that

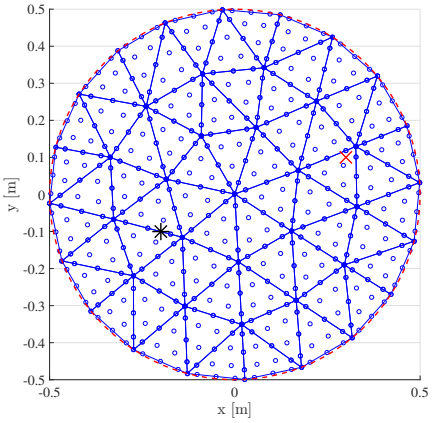

FIG. 5. (Color online) Mesh of the 2D circular domain, made using distmesh.[65] The mesh consists of 60 elements, 521 DOF's. The circumference error for the straight-sided mesh is 0.41% and the interior surface area error is 1.64%. The source location is shown with a red cross ($(s_x, s_y) = (0.3, 0.1)$) and the receiver location is shown with a black star ($(r_x, r_y) = (-0.2, -0.1)$).

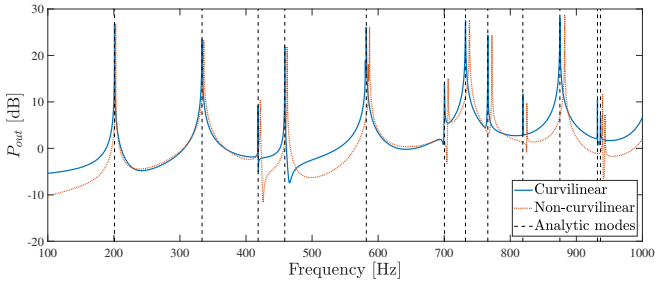

FIG. 6. (Color online) Simulated frequency responses in the 2D circular domain, with and without curvilinear boundary elements. Analytic modes are dashed vertical lines, calculated using Green's function.[66]

$N_{\text{el}} = 24, 12, 6, 4$ per dimension, in a uniform hexahedral mesh, for $P = 1, 2, 4, 6$, respectively. The spatial resolution in all cases corresponds to roughly 8.6 PPW at 1 kHz. The initial condition is a Gaussian pulse with spatial variance $\sigma = 0.2$ m^2, the simulation time is 3 s and the time step size is determined using Eq. (34) with $C_{\text{CFL}} = 0.2$. The simulated frequency responses are shown in Fig. 8. The figure shows how the usage of high-order polynomial basis functions results in a closer match to the analytic solution, for the given fixed spatial resolution. As the polynomial order is increased, the valid frequency range of the simulation is effectively extended. The numerical error manifests itself both via mistunings of the exact modes due to dispersion, mismatch of modal frequency amplitudes and as noise in the valleys between modal frequencies.

The dispersion error is analyzed further in Fig. 9, where the numerical modal frequencies are compared

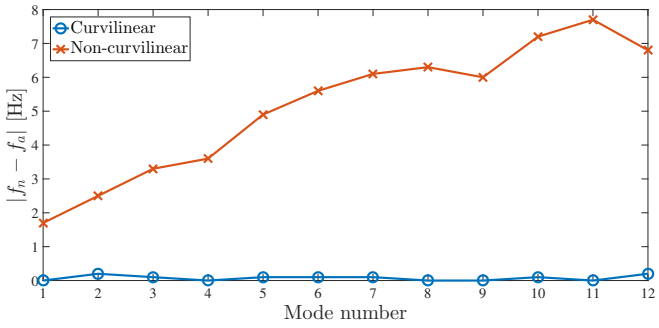

FIG. 7. (Color online) Error in simulated modal frequencies for the 2D cirular domain case.

against the analytic modal frequencies. The difference is constant and smaller than 0.4 Hz for the first 35 modes for $P = 4$ and $P = 6$, but increases fast with frequency for $P = 1$, being 0.7 Hz for the 1st mode to 39.0 Hz for the 15th mode. The numerical dissipation in the scheme for this test case, calculated using Eq. (37), is shown in Fig. 10. The dissipation is found to be very low, less than 0.03% in all cases.

C. Single 3D reflection from an impedance boundary

In order to assess how accurately the proposed scheme represents locally reacting, frequency dependent impedance boundary conditions, a single reflection of a spherical wave hitting such a boundary is studied. For this case, an analytic solution exists.[68] The wave reflection is studied under two different boundary conditions. In both cases the boundary is modelled as a porous material having flow resistivity of $\sigma_{\text{mat}} = 10000$ Nsm^{-4}, but having thickness of either $d_{\text{mat}} = 0.02$ m or $d_{\text{mat}} = 0.05$ m. The surface impedance of these materials are estimated using Miki's model[46] and mapped to a six pole rational function using a vector fitting algorithm.[69] Fig. 11 shows the surface admittance of these two materials and the resulting rational function approximation. Using six poles is sufficient to perfectly capture the real and imaginary part of the admittance curves. Fig. 12 shows the corresponding absorption coefficients of the two materials.

A large 3D domain is used for the simulation and the resulting impulse response is windowed such that no parasitic reflections from other surfaces influence the simulated response. The source is located 2 m from the impedance boundary and the receiver is located 1 m from the boundary, right between the source and the boundary. A basis order of $P = 4$ is used and a high spatial resolution is employed, roughly 14 PPW at 1 kHz, ensuring minimal numerical errors in the frequency range of interest. The initial condition is again a Gaussian pulse spatial variance $\sigma = 0.2$ m^2.

The resulting complex pressure is shown in the frequency domain in Fig. 13. The simulated pressure matches the analytic solution perfectly, both in terms

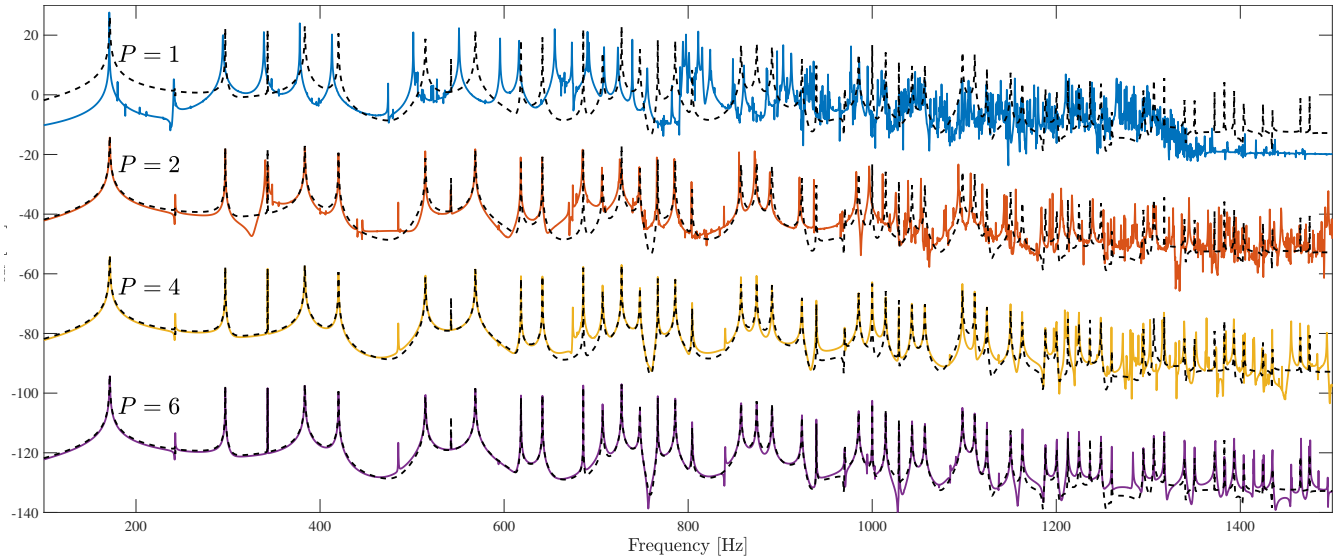

FIG. 8. (Color online) Simulated frequency responses of a cube shaped room with rigid boundaries for basis orders $P = 1, 2, 4, 6$, while using a fixed spatial resolution (15,625 DOF's). The analytic solution is the dashed curve. The source location is $(s_x, s_y, s_z) = (0.25, 0.75, 0.60)$ and the receiver location is $(r_x, r_y, r_z) = (0.85, 0.30, 0.80)$. The responses have been offset by 40 dB to aid visibility.

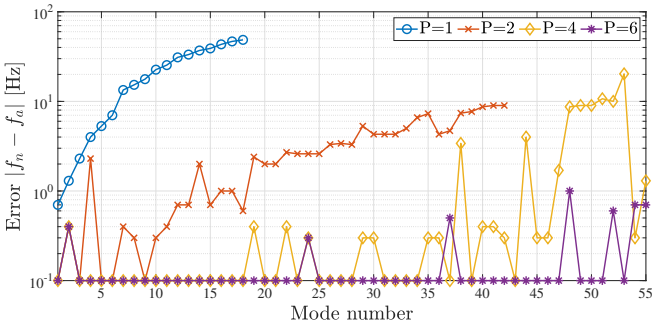

FIG. 9. (Color online) Error in simulated modal frequencies for the cube shaped room with rigid boundaries case.

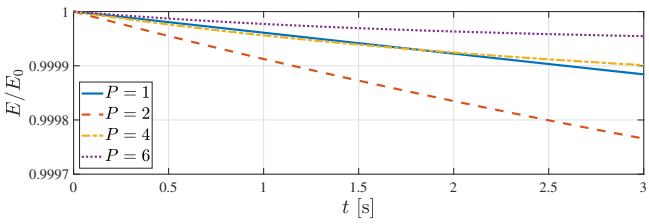

FIG. 10. (Color online) Numerical dissipation for the cube shaped room with rigid boundaries case.

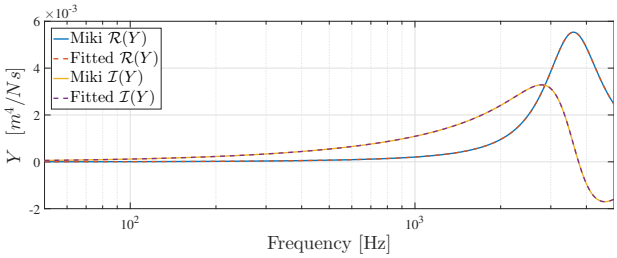

a) $d_{\text{mat}} = 0.02$ m.

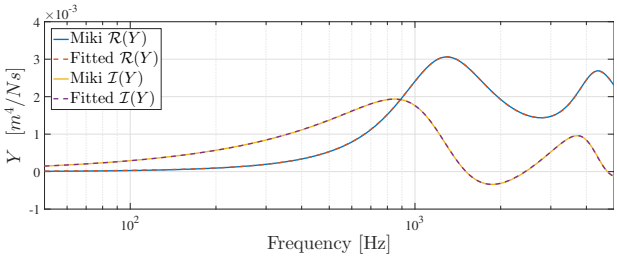

b) $d_{\text{mat}} = 0.05$ m.

FIG. 11. (Color online) Rational function fitting of the normal incidence admittance of the two porous materials used in the single reflection test case.

of amplitude and phase, for both boundary condition tested, thus illustrating the high precision of the method used for representing locally reacting, frequency dependent boundary conditions in the numerical scheme.

D. 3D room with frequency dependent boundary conditions

As a final test case, an impulse response in the $1 \times 1 \times 1$ m cube shaped room is simulated under frequency dependent boundary conditions, where one of the

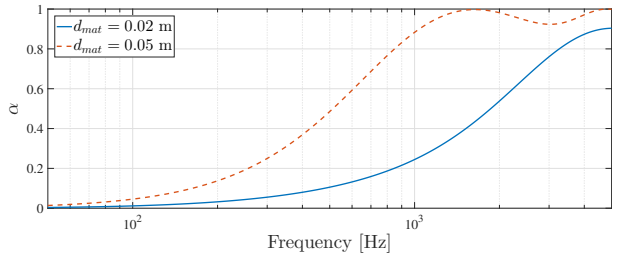

FIG. 12. (Color online) Normal incidence absorption coefficient of the two porous materials used in the single reflection test case.

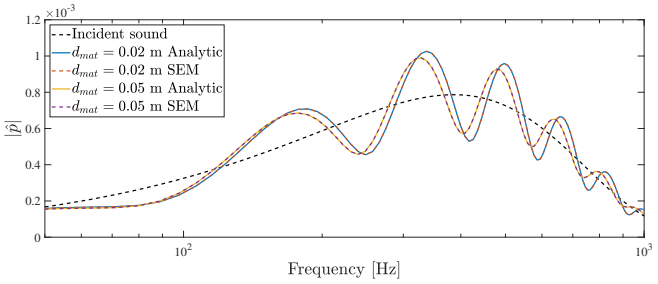

a) Amplitude.

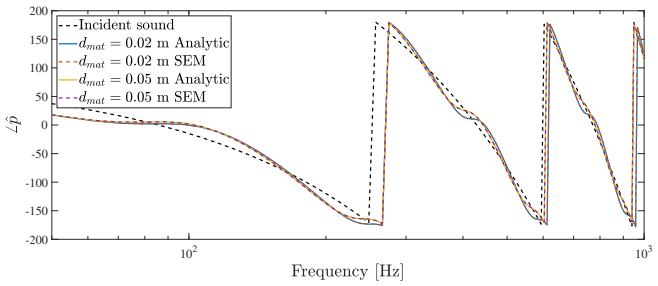

b) Phase.

FIG. 13. (Color online) Simulated complex pressure of a single reflection from a locally reacting, frequency dependent impedance boundary, compared with an analytic solution.

boundary surfaces of the room is made to be covered with a porous material. The same two materials considered in Sec. V C are used again in this test case. The basis order used in the simulation is $P = 4$, the source and receiver positions, the initial condition and C_{CFL} are the same as in the tests in Sec. V B, but the spatial resolution has been increased to $N_{\text{el}} = 10$ elements per dimension, corresponding to roughly 14 PPW at 1 kHz.

The resulting frequency responses are shown in Fig. 14. The figure shows how, in the presence of the porous material, the modal frequency peaks have both decreased in amplitude, due to sound absorption at the boundary, and shifted in frequency, due to a phase shift at the boundary, when compared to the perfectly rigid boundary case. The frequency dependent behavior of the porous material is evident in the frequency response. At lower frequencies the modal peaks are less dampened compared to the higher frequencies, and clearly the $d_{\text{mat}} = 0.05$ m material is more absorptive than the $d_{\text{mat}} = 0.02$ m material.

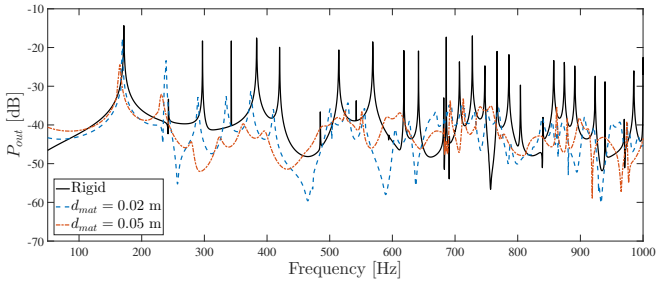

FIG. 14. (Color online) Simulated frequency responses of a cube shaped room, with five rigid surfaces and one surface covered with a porous material. The case where all surfaces are rigid is also shown. Basis order $P = 4$ is used in the simulation.

VI. CONCLUSION

In this study, a time domain numerical scheme adapted for room acoustic simulations, based on a spectral element method in space and an implicit-explicit Runge-Kutta method in time, has been developed and evaluated. The main benefits of this scheme are its high-order accuracy, combined with its geometrical flexibility, allowing for accurate and cost-effective room acoustic simulations of complex geometries.

The results presented in this study show that there is a significant improvement in cost-efficiency and accuracy when high-order basis functions are used. This has been shown both via a multi-modal, spatio-temporal dispersion analysis and via various three dimensional numerical experiments. Furthermore, it has been shown how the high geometric flexibility of the SEM makes it possible to simulate domains with curved geometries with very high accuracy. Errors in estimating modal frequencies due to poor representation of curved geometries when using straight-sided mesh elements are effectively mitigated by using curvilinear boundary elements.

The presented method for representing locally reacting, frequency dependent impedance boundary conditions is found to be highly accurate, with a perfect match seen between analytic solutions and simulations, in the case of a normal incidence spherical wave being reflected from a impedance boundary. The solution of the boundary ADE's comes with minimal additional computational cost and is carried out implicitly, thus the solution of these equations has no influence over the stability conditions of the scheme.

The fact that room acoustic simulations involve broad frequency ranges, tight error tolerances, long simulation times and large, complex 3D domains, make the

proposed scheme particularly suitable for room acoustic simulations where high precision is important. As the simulation time gets longer, the frequency range gets broader and the desired accuracy gets higher, the benefits of using high-order methods relative to low-order methods become greater.

ACKNOWLEDGMENTS

This research has been partially funded by the Innovation Fund in Denmark. Benchmarking has been done using the infrastructure at the DTU Computing Center.

[1]S. Pelzer, L. Aspock, D. Schroder, and M. Vorlander. Integrating real-time room acoustics simulation into a CAD modeling software to enhance the architectural design process. *Buildings*, 4(2):113–138, 2014.

[2]R. Mehra, A. Rungta, A. Golas, M. Lin, and D. Manocha. WAVE: Interactive wave-based sound propagation for virtual environments. *IEEE Trans. Vis. Comp. Graph.*, 21(4):434–442, 2015.

[3]N. Raghuvanshi, A. Allen, and J. Snyder. Numerical wave simulation for interactive audio-visual applications. *J. Acoust. Soc. Am.*, 139(4):2008–2009, 2016.

[4]M. Aretz and M. Vorlander. Combined wave and ray based room acoustic simulations of audio systems in car passenger compartments, part i: Boundary and source data. *Appl. Acoust.*, 76:82–99, 2014.

[5]V. Valimaki, J. D. Parker, L. Savioja, J. O. Smith, and J. S. Abel. Fifty years of artificial reverberation. *IEEE Trans. Audio, Speech, Lang. Proc.*, 20(5):1421–1448, 2012.

[6]J. Xia, B. Xu, S. Pentony, J. Xu, and J. Swaminathan. Effects of reverberation and noise on speech intelligibility in normal-hearing and aided hearing-impaired listeners. *J. Acoust. Soc. Am.*, 143(3):1523–1533, 2018.

[7]M. R. Schroeder and K. H. Kuttruff. On frequency response curves in rooms. Comparison of experimental, theoretical, and Monte Carlo results for the average frequency spacing between maxima. *J. Acoust. Soc. Am.*, 34(1):76–80, 1962.

[8]A. Krokstad, S. Strom, and S. Soersdal. Calculating the acoustical room response by the use of a ray tracing technique. *J. Sound Vib.*, 8(1):118–125, 1968.

[9]L. Savioja and U. P. Svensson. Overview of geometrical room acoustic modeling techniques. *J. Acoust. Soc. Am.*, 138(2):708–730, 2015.

[10]A. Kulowski. Algorithmic representation of the ray tracing technique. *Appl. Acoust.*, 18(6):449–469, 1985.

[11]H. Lee and B.-H. Lee. An efficient algorithm for the image model technique. *Appl. Acoust.*, 24(2):87–115, 1988.

[12]S. Laine, S. Siltanen, T. Lokki, and L. Savioja. Accelerated beam tracing algorithm. *Appl. Acoust.*, 70(1):172–181, 2009.

[13]Y. W. Lam. Issues for computer modelling of room acoustics in non-concert hall settings. *Acoust. Sci. Tech.*, 26(2):145–155, 2005.

[14]J. LoVetri, D. Mardare, and G. Soulodre. Modeling of the seat dip effect using the finite-difference time-domain method. *J. Acoust. Soc. Am.*, 100(4):2204–2212, 1996.

[15]T. J. Cox and P. D'Antonio. *Acoustic absorbers and diffusers: theory, design and application*. Routledge Taylor & Francis, 3rd edition, 2016. Ch. 13.

[16]M. L. S. Vercammen. *Sound concentration caused by curved surfaces*. PhD thesis, Eindhoven University of Technology, The Netherlands, 2011.

[17]M. Vorlander. Computer simulations in room acoustics: Concepts and uncertainties. *J. Acoust. Soc. Am.*, 133(3):1203–1213, 2013.

[18]D. Botteldooren. Finite-difference time-domain simulation of low-frequency room acoustic problems. *J. Acoust. Soc. Am.*, 98(6):3302–3308, 1995.

[19]J. A. Hargreaves and T. J. Cox. A transient boundary element method model of Schroeder diffuser scattering using well mouth impedance. *J. Acoust. Soc. Am.*, 124(5):2942–2951, 2008.

[20]T. Okuzono, T. Otsuru, R. Tomiku, and N. Okamoto. A finite-element method using dispersion reduced spline elements for room acoustics simulation. *Appl. Acoust.*, 79:1–8, 2014.

[21]R. Mehra, N. Raghuvanshi, L. Antani, A. Chandak, S. Curtis, and D. Manocha. Wave-based sound propagation in large open scenes using an equivalent source formulation. *ACM Trans. Graph.*, 32(2):19:1–19:13, 2013.

[22]S. Bilbao. Modeling of complex geometries and boundary conditions in finite difference/finite volume time domain room acoustics simulation. *IEEE Trans. Audio, Speech, Lang. Proc.*, 21(7):1524–1533, 2013.

[23]M. Hornikx, T. Krijnen, and L. van Harten. openPSTD: The open source pseudospectral time-domain method for acoustic propagation. *Comp. Phys. Comm.*, 203:298–308, 2016.

[24]M. Vorlander. *Auralization: Fundamentals of Acoustics, Modelling, Simulation, Algorithms and Acoustic Virtual Reality*. Springer, 2008. Ch. 10.

[25]L. Savioja. Real-time 3D finite-difference time-domain simulation of low-and mid-frequency room acoustics. In *13th International Conference on Digital Audio Effects*, volume 1, 2010.

[26]A. Southern, S. Siltanen, D. T. Murphy, and L. Savioja. Room impulse response synthesis and validation using a hybrid acoustic model. *IEEE Trans. Audio, Speech, Lang. Proc.*, 21(9):1940–1952, 2013.

[27]R. P. Munoz and M. Hornikx. Hybrid Fourier pseudospectral/discontinuous Galerkin time-domain method for wave propagation. *J. Comp. Phys.*, 348:416–432, 2017.

[28]H.-O. Kreiss and J. Oliger. Comparison of accurate methods for the integration of hyperbolic equations. *Tellus*, 24(3):199–215, 1972.

[29]J. van Mourik and D. Murphy. Explicit higher-order FDTD schemes for 3D room acoustic simulation. *IEEE Trans. Audio, Speech, Lang. Proc.*, 22(12):2003–2011, 2014.

[30]B. Hamilton and S. Bilbao. FDTD methods for 3-D room acoustics simulation with high-order accuracy in space and time. *IEEE Trans. Audio, Speech, Lang. Proc.*, 25(11):2112–2124, 2017.

[31]A. T. Patera. A spectral element method for fluid dynamics: Laminar flow in a channel expansion. *J. Comp. Phys.*, 54(3):468–488, 1984.

[32]G.E. Karniadakis and S.J. Sherwin. *Spectral/hp Element Methods for Computational Fluid Dynamics*. Oxford University Press, 2nd edition, 2005.

[33]D. Kopriva. *Implementing Spectral Methods for Partial Differential Equations*. Springer, 2009.

[34]A.P. Engsig-Karup, C. Eskilsson, and D. Bigoni. A stabilised nodal spectral element method for fully nonlinear water waves. *J. Comp. Phys.*, 318:1–21, 2016.

[35]G. Seriani. A parallel spectral element method for acoustic wave modeling. *J. Comp. Acoust.*, 05(01):53–69, 1997.

[36]S. Airiau, M. Azaiez, F.B. Belgacem, and R. Guivarch. Parallelization of spectral element methods. In J. M. L. M. Palma, A. A. Sousa, J. Dongarra, and V. Hernandez, editors, *High Performance Computing for Computational Science — VECPAR 2002*, pages 392–403. Springer, 2003.

[37]C. A. Kennedy and M. H. Carpenter. Additive Runge-Kutta schemes for convection-diffusion-reaction equations. *Appl. Num. Math.*, 44(1):139–181, 2003.

[38]M. Hornikx. Ten questions concerning computational urban acoustics. *Build. Enviro.*, 106:409–421, 2016.

[39]S. Bilbao, B. Hamilton, J. Botts, and L. Savioja. Finite volume time domain room acoustics simulation under general impedance boundary conditions. *IEEE Trans. Audio, Speech, Lang. Proc.*,

24(1):161–173, 2016.

[40]C.-W. Shu. Essentially non-oscillatory and weighted essentially non-oscillatory schemes for hyperbolic conservation laws. In A. Quarteroni, editor, *Advanced Numerical Approximation of Nonlinear Hyperbolic Equations*, pages 325–432. Springer, 1998.

[41]C.-W. Shu. High-order finite difference and finite volume WENO schemes and discontinuous Galerkin methods for CFD. *Int. J. Comp. Fluid Dynamics*, 17(2):107–118, 2003.

[42]N. Atalla and F. Sgard. *Finite Element and Boundary Methods in Structural Acoustics and Vibration*. CRC Press, 1st edition, 2015. Ch. 7.

[43]I. Babuska and B.Q. Guo. The h, p and h-p version of the finite element method; basis theory and applications. *Adv. Eng. Softw.*, 15(3):159–174, 1992.

[44]J. S. Hesthaven and T. Warburton. *Nodal Discontinuous Galerkin Methods—Algorithms, Analysis, and Applications*. Springer, 2008. Ch. 1,3,4,6,9 and 10.

[45]A. Richard, E. Fernandez-Grande, J. Brunskog, and C.-H. Jeong. Estimation of surface impedance at oblique incidence based on sparse array processing. *J. Acoust. Soc. Am.*, 141(6):4115–4125, 2017.

[46]Y. Miki. Acoustical properties of porous materials - modifications of Delany-Bazley models. *J. Acoust. Soc. Jap.*, 11(1):19–24, 1990.

[47]R. Troian, D. Dragna, C. Bailly, and M.-A. Galland. Broadband liner impedance eduction for multimodal acoustic propagation in the presence of a mean flow. *J. Sound Vib.*, 392:200–216, 2017.

[48]P. Cazeaux and J. S. Hesthaven. Multiscale modelling of sound propagation through the lung parenchyma. *ESAIM: M2AN*, 48(1):27–52, 2014.

[49]A. Taflove and S. C. Hagness. *Computational Electrodynamics: The Finite-Difference Time-Domain Method*. Artech House, Inc., 3 edition, 2013. Ch. 9.

[50]M. Dubiner. Spectral methods on triangles and other domains. *J. Sci. Comp.*, 6(4):345–390, 1991.

[51]T. Okuzono, T. Yoshida, K. Sakagami, and T. Otsuru. An explicit time-domain finite element method for room acoustics simulations: Comparison of the performance with implicit methods. *Appl. Acoust.*, 104:76–84, 2016.

[52]M. Ainsworth and H. Wajid. Dispersive and dissipative behavior of the spectral element method. *SIAM J. Num. Anal.*, 47(5):3910–3937, 2009.

[53]S. Sherwin. Dispersion analysis of the continuous and discontinuous Galerkin formulations. In B. Cockburn, G. E. Karniadakis, and C.-W. Shu, editors, *Discontinuous Galerkin Methods*, pages 425–431. Springer, 2000.

[54]G. Gassner and D. Kopriva. A comparison of the dispersion and dissipation errors of Gauss and Gauss-Lobatto discontinuous Galerkin spectral element methods. *SIAM J. Sci. Comp.*, 33(5):2560–2579, 2011.

[55]G. Seriani and S.P. Oliveira. DFT modal analysis of spectral element methods for acoustic wave propagation. *J. Comp. Acoust.*, 16(04):531–561, 2008.

[56]Fang Q. Hu, M.Y. Hussaini, and P. Rasetarinera. An analysis of the discontinuous Galerkin method for wave propagation problems. *J. Comp. Phys.*, 151(2):921–946, 1999.

[57]S. P. Oliveira. On multiple modes of propagation of high-order finite element methods for the acoustic wave equation. In M. L. Bittencourt, N.A. Dumont, and J. S. Hesthaven, editors, *Spectral and High Order Methods for Partial Differential Equations ICOSAHOM 2016*, pages 509–518. Springer, 2017.

[58]G. Seriani and S. P. Oliveira. Optimal blended spectral-element operators for acoustic wave modeling. *Geophysics*, 72(5):SM95–SM106, 2007.

[59]Y. Geng, G. Qin, J. Zhang, W. He, Z. Bao, and Y. Wang. Space-time spectral element method solution for the acoustic wave equation and its dispersion analysis. *Acoust. Sci. and Tech.*, 38(6):303–313, 2017.

[60]J. Yu, C. Yan, and Z. Jiang. Effects of artificial viscosity and upwinding on spectral properties of the discontinuous Galerkin method. *Comp. Fluids*, 175:276–292, 2018.

[61]J. Saarelma, J. Botts, B. Hamilton, and L. Savioja. Audibility of dispersion error in room acoustic finite-difference time-domain simulation as a function of simulation distance. *J. Acoust. Soc. Am.*, 139(4):1822–1832, 2016.

[62]C. A. Felippa, Q. Guo, and K.C. Park. Mass matrix templates: General description and 1D examples. *Arch. Comp. Meth. Eng.*, 22(1):1–65, 2015.

[63]I. Fried and D. S. Malkus. Finite element mass matrix lumping by numerical integration with no convergence rate loss. *Int. J. Sol. Struct.*, 11(4):461–466, 1975.

[64]S. Jund and S. Salmon. Arbitrary high-order finite element schemes and high-order mass lumping. *Int. J. Appl. Math. Comp. Sci.*, 17(3):375–393, 2007.

[65]P.-O. Persson and G. Strang. A simple mesh generator in Matlab. *SIAM Review*, 46(2):329–345, 2004.

[66]F. Jacobsen and P. Juhl. *Fundamentals of General Linear Acoustics*. Wiley, 2013. Ch. 7.

[67]S. Sakamoto. Phase-error analysis of high-order finite difference time domain scheme and its influence on calculation results of impulse response in closed sound field. *Acoust. Sci. Tech.*, 28(5):295–309, 2007.

[68]S.-I. Thomasson. Reflection of waves from a point source by an impedance boundary. *J. Acoust. Soc. Am.*, 59(4):780–785, 1976.

[69]B. Gustavsen and A. Semlyen. Rational approximation of frequency domain responses by vector fitting. *IEEE Trans. Pow. Del.*, 14(3):1052–1061, 1999.